We are IntechOpen,
the world's leading publisher of
Open Access books
Built by scientists, for scientists

4,800
Open access books available

122,000
International authors and editors

135M
Downloads

154
Countries delivered to

Our authors are among the

TOP 1%
most cited scientists

12.2%
Contributors from top 500 universities

BOOK CITATION INDEX
CLARIVATE ANALYTICS
INDEXED

WEB OF SCIENCE™

Selection of our books indexed in the Book Citation Index
in Web of Science™ Core Collection (BKCI)

Interested in publishing with us?
Contact book.department@intechopen.com

Numbers displayed above are based on latest data collected.
For more information visit www.intechopen.com

Electrochemical Synthesis of Rare Earth Ceramic Oxide Coatings

Teresa D. Golden, Yajuan Shang, Qi Wang and
Ting Zhou

Additional information is available at the end of the chapter

Abstract

Rare earth ceramic oxides are used in several applications including, phosphors, gas sensors, fuel cells, catalytic converters, and corrosion protection. These materials exhibit attractive properties such as fracture toughness, stiffness, and high strength-to-weight ratios. Synthesis of rare earth oxides includes a long list of techniques, but electrodeposition is one that has not been used as extensively as other techniques. This chapter discusses in detail the electrochemical synthesis of lanthanum, cerium, and praseodymium oxides. The physical and chemical properties of the electrodeposited oxides are characterized by x-ray diffraction, scanning electron microscopy, x-ray photoelectron spectroscopy, and other techniques. The electrochemical synthesis and post-treatment of other rare earth oxides, such as gadolinium, terbium, samarium, neodymium, europium, and dysprosium oxides are also covered in this chapter. Two main mechanisms of electrodeposition for rare earth oxides are discussed in detail.

Keywords: Electrodeposition, rare earth oxides, cathodic, anodic

1. Introduction

Ceramic oxides (M_xO_y) typically have a combination of properties that make them attractive for many applications. These oxides exhibit fracture toughness and hardness, and can be used to make low weight composites of high strength. Ceramic oxides can also be used as protection coatings because of their interesting corrosion inhibiting properties [1-3]. These

structural ceramics can be used to coat specific components exposed to extreme conditions, such as high temperature, high stress, or high friction. Of the ceramic oxides, rare earth oxides (REOs) are interesting materials and are a type of ceramic oxide that has many promising properties. Rare earth oxides can be used to color glass, for example, Er_2O_3 adds a light pink color while Sm_2O_3 produces a yellow color [4, 5]. REOs are used in the making of phosphors or fluorescent lighting [6, 7]. Rare earth oxides such as cerium oxide have also been important in automotive catalytic converters [8]. The most common stoichiometry for rare earth oxides is R_2O_3; however other compounds containing Ce, Pr, or Tb can exhibit several oxide phases, RO_x (1.5 < x < 2) and compounds like CeO_2, Pr_6O_{11}, and Tb_4O_7 are common. Applications for rare earth oxide coatings include gas sensors [9, 10], fuel cells [11, 12], catalysis [13, 14], and corrosion protection [1, 15-18].

There is a long list of processing techniques for producing rare earth oxides including spray hydrolysis, pulsed laser deposition, chemical vapor deposition, solid state reactions, sol–gel method, and melt infiltration [19-24]. However, electrochemical synthesis has not been used extensively to deposit rare earth oxide coatings. The electrodeposition mechanism can be complex for many of the reactions and present a formidable challenge. In fact the majority of the electrodeposition work has focused on cerium oxide coatings and powders [25-28]. Typically, the redox potential for the rare earth oxides is not readily accessible in aqueous solutions, making synthesis difficult. But electrochemical deposition offers several advantages including low processing temperature, control of the driving force, and deposition onto various shapes [29-31]. This chapter covers the electrochemical deposition (not electrophoretic or soaking methods) of rare earth oxides as films for various applications.

2. Electrochemical synthesis techniques for ceramic oxides

For the deposition of ceramic oxides, there are three main methods. These include electrophoretic, electrolytic (base generation), and direct electrodeposition. Electrophoretic deposition occurs when a high electric field is applied in a solution that contains suspended particles. The charged particles in solution migrate to and then are deposited on the electrode surface. Typically, much higher voltages or currents are used to drive the ions in solution during this deposition compared to electrodeposition. Electrophoretic deposition tends to give thicker coatings than other techniques.

Electrolytic deposition occurs when cathodic reactions produce colloidal particles in solution next to the electrode surface. This method has an electrogeneration of base or local change of pH at the electrode surface. The solution contains metal salts or metal complexes. This may result in powdery or loosely adherent coatings. The cathodic electrodeposition or base generation method for synthesizing oxides was first described by Switzer [32]. The local increase in pH happens either by consumption of hydronium ions or production of hydroxide ions. Depending on the species in solution, both of these mechanisms may be occurring. The most likely reactions include [33]:

$$H^+ + e^- \rightarrow H_{ads} \tag{1}$$

$$2H^+ + 2e^- \rightarrow H_2 \tag{2}$$

$$2H_2O + 2e^- \rightarrow H_2 + 2OH^- \tag{3}$$

$$O_2 + 2H_2O + 4e^- \rightarrow 4OH^- \tag{4}$$

If a nitrate salt is present in the solution then hydronium ions can be consumed or hydroxide ions produced by:

$$NO_3^- + 2H^+ + 2e^- \rightarrow NO_2^- + H_2O \tag{5}$$

$$NO_3^- + 10H^+ + 8e^- \rightarrow NH_4^+ + 3H_2O \tag{6}$$

$$NO_3^- + H_2O + 2e^- \rightarrow NO_2^- + 2OH^- \tag{7}$$

$$NO_3^- + 7H_2O + 8e^- \rightarrow NH_4^+ + 10OH^- \tag{8}$$

With any of these reactions, the local pH at the electrode surface is increased and can be as high as 11–12 compared to the lower pH in the bulk of the solution.

Direct electrodeposition occurs when there is a direct oxidation or reduction (exchange of electrons) between the metal ion or metal ion complex and electrode to produce the metal oxide on the surface. This method is typical for electrochemical reactions, such as reduction of metal ions in solution to produce pure metal on an electrode surface (plating).

In this chapter, we cover only electrolytic and direct electrodeposition for the production of rare earth oxide coatings. The oxides or hydroxides of lanthanum, cerium, praseodymium, neodymium, samarium, europium, gadolinium, terbium, and dysprosium have been electrochemically produced. To date, the bulk of the electrochemical literature covers cerium oxide (CeO_2), about 40:1 compared to the other rare earth oxides. It must be noted that in aqueous solutions, the lanthanide hydroxides are stable in alkaline solutions but return to their corresponding cations in acid solutions [34]. This is true for all the lanthanide series; however, a few do have a stable oxide that may be accessible during deposition under the correct conditions. These include CeO_2, PrO_2, NdO_2, and TbO_2. In practice, this means that most of the rare earths are deposited as hydroxides or hydrated oxide species and post-treatment is needed

to produce the desired stoichiometry. We will make note of this in our discussions when applicable for each section.

3. Electrochemical synthesis of lanthanum oxide (La₂O₃)

Lanthanum oxide (La_2O_3) has been utilized in several technological applications, such as light-emitting phosphors, solid oxide fuel cells, catalysis, automobile exhaust-gas converters, and sorbent materials [35-39]. There are only a few papers reporting the attempt to electrodeposit lanthanum oxides from aqueous solutions [39-42]. In practice, La_2O_3 has not been deposited directly using electrodeposition. However, lanthanum hydroxide, $La(OH)_3$, has been electrochemically deposited. Bocchetta et al. first showed that it was possible to obtain $La(OH)_3$ from a solution of lanthanum nitrate using galvanostatic deposition at a cathodic current of 1 mA/cm² [40]. They obtained nanowires on an Al substrate, and the authors proposed that deposition occurred through a base generation mechanism. Yao et al. did a similar type of deposition using lanthanum nitrate and ammonia nitrate to obtain $La(OH)_3$ nanorods on a copper substrate [41]. Like previous authors, they also proposed a base generation mechanism in which hydroxide ions are formed from the nitrate and water reduction:

$$NO_3^- + H_2O + 2e^- \rightarrow NO_2^- + 2OH^- \tag{9}$$

$$2H_2O + 2e^- \rightarrow H_2 + 2OH^- \tag{10}$$

However, by studying the SEM images along the potential-time curve, they also proposed that the evolution of hydrogen (reaction 10) was important in obtaining the nanorod formation. The H_2 bubbles acted as a dynamic template forcing the nanorods in a vertical growth direction through the pressure of the bubbles.

The formation of La_2O_3 from $La(OH)_3$ was first done by Liu et al. [42]. They fabricated $La(OH)_3$ nanospindles and nanorods on F-doped SnO_2 substrates using galvanostatic deposition from a bath containing 0.01 M $La(NO_3)_3$ and 30-50% DMSO. After obtaining $La(OH)_3$ nanorods, the coating was sintered at 690 ℃. A pure hexagonal structure of La_2O_3 was obtained as revealed by the XRD pattern. The percentage of DMSO in the deposition solution affected the nanostructure of the deposits. Lower concentration produced nanorods, higher concentration produced nanospindles.

Other researchers also obtained nanorods, nanospindles, and nanocapsules of La_2O_3 by electrodeposition of $La(OH)_3$ using the base generation method and then sintering [43-45]. However, it was shown by CHN analysis and FTIR that nitrates were codeposited into the $La(OH)_3$ hexagonal lattice. A sharp peak at 1383 cm⁻¹ in the FTIR spectra for the hydroxide sample is due to the vibration modes of NO_3^- ions intercalated in the deposit structure during electrodeposition. After sintering, no nitrates were present in the coating. Very nice vertically

aligned uniform nanorods were prepared of $La(OH)_3$ and La_2O_3 using a pulsed electrodeposition method followed by heat treatment [43]. In conclusion, while La_2O_3 has not been directly electrodeposited onto various substrates, $La(OH)_3$ can be deposited from a nitrate solution using the base generation method and then heat treated (typically ~600 ℃) to obtain La_2O_3.

4. Electrochemical synthesis of cerium oxides

Cerium oxide (CeO_2) is of interest in the area of catalysis [46]. Much effort has been dedicated to studying the role of ceria in several well-established industrial processes such as three-way-catalysis (TWC) systems and fluid catalytic cracking (FCC) systems, where CeO_2 is a key component in catalyst formulation. Cerium oxide is used to remove automotive exhaust gases such as NO, CO, and CH_x, and to eliminate SO_x and NO_x from fuel gases [47]. Ceria also demonstrates catalytic function in the removal of soot from diesel engine exhaust, elimination of organics from wastewaters (catalytic wet oxidation), and cracking of heavy oil in zeolite. In addition, CeO_2 is a semiconducting and ionic-conducting oxide. It can substitute for ZrO_2 as the electrolyte material in solid oxide fuel cell (SOFC) systems and has been regarded as a model system for mixed ionic/electronic conductor investigations [48].

Particle size plays a significant role in the unique properties and applications of cerium oxide. Generally speaking, the smaller the particle size, the lower the packing porosity and the higher the surface area. Catalytic activity and electrical conductivity of crystalline cerium oxide are dependent on particle size, where electronic conductivity predominates in the nanocrystalline phase and ionic conductivity mainly controls the microcrystalline structure [49]. The nanocrystalline phase of cerium oxide is favorable for formation of a nonstoichiometric structure due to reduced enthalpy of defect formation and propensity for oxygen vacancies. The fluorite structure of CeO_2 favors oxygen vacancy formation in the lattice, enhancing the catalytic reactivity of CeO_2 in TWC, FCC, and other gas phase oxidation and reduction reactions [50]. Nanocrystalline cerium oxide improves catalytic properties significantly, leading to higher conversion of carbon monoxide to dioxide and sulfur dioxide to elemental sulfur at lower temperatures. The improved catalytic reactivity was also demonstrated in the oxidation of methane [51-53]. The sinterability of crystalline cerium oxide increases with decreasing particle size. The reduction of sintering temperature for nanocrystalline cerium oxide overcomes processing temperature difficulty and makes it a promising candidate as an electrolyte in solid oxide fuel cells [52, 53]. Ceria can also be used for corrosion protection on a number of different substrates [54-56].

Cerium typically forms two types of oxides, cerium dioxide (CeO_2) and cerium sesquioxide (Ce_2O_3). Cerium sesquioxide (Ce_2O_3) has two structural forms, hexagonal (A-type) and cubic (C-type). Cerium oxide (CeO_2) has a fluorite (CaF_2) structure (fcc) with space group Fm3m. Figure 1 shows the structure of the stoichiometric CeO_2 with the oxygen (represented by circles) four coordinated and the cerium (represented by solid balls) eight coordinated. The cerium atom is at the center of the tetrahedron and the tetrahedral corners are occupied by oxygen atoms. Cerium oxide can exist as a non-stoichiometric oxide, that is a mixture of Ce(III) oxide

and Ce(IV) oxide, while still retaining the fluorite cubic structure. The coatings can be easily identified by x-ray diffraction (XRD) analysis.
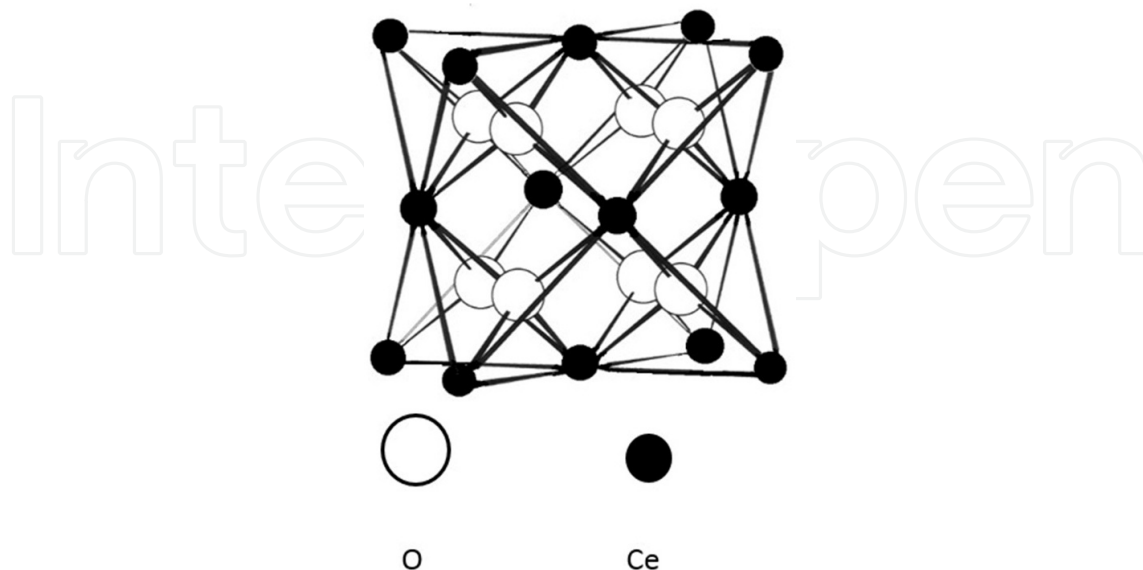

Figure 1. Fluorite structure of cerium oxide.

For the electrodeposition of rare earth oxides, cerium oxide is by far the most studied. It is also one of the few that has been deposited by both electrolytic (base generation) and direct electrodeposition. Cathodic electrodeposition (i.e., base generation electrochemical method) was first introduced for the plating of cerium oxide films [32]. Switzer et al. used this method to produce cerium oxide films and powders [57, 58]. Crystalline, randomly oriented cerium oxide coatings were deposited galvanostatically from a cerium nitrate solution. During the synthesis, the pH changed from ~ 4.5 to 7.5, showing that base was generated during deposition.

An in-depth study was done by Aldykiewicz et al. to understand the base generation mechanism for CeO_2 deposition [59]. They proposed a mechanism involving oxygen to produce an oxidizing agent (i.e., H_2O_2) for Ce(III) to Ce(IV) formation. With an oxidant available in the system, cerium oxide film formation was accomplished through a four- or two-electron process to a hydroxide intermediate. A critical pH value above 8.7 was needed to keep the cerium hydroxide ions stable in solution. The final step was the precipitation of CeO_2 onto the electrode surface. This mechanism was supported by rotation disk electrode experiments and XANES studies. Li et al. studied the mechanism proposed by Aldykiewicz with in situ atomic force microscopy technique (AFM) and concluded that a cerium hydroxide species is produced at the electrode surface with CeO_2 forming nuclei out of this hydroxide "gel". The rate-determining step for this mechanism is then the nucleation and growth of the CeO_2 crystals [60-62].

Zhitomirsky also proposed that hydrogen peroxide plays a dominant role in the two-electron reduction process for the earlier mentioned mechanism [63-65]. He used H_2O_2 as an additive

for the cathodic electrodeposition of CeO_2 and Gd-doped ceria films from aqueous and mixed alcohol–water solutions of cerium chloride or nitrate. He then proposed that a $CeO_2.nH_2O$ or $Ce(OH)_3OOH$ deposit formed via two- or four-electron reduction, owing to the participation of hydrogen peroxide in the oxidation step. Zhitomirsky noticed that there was always a lot of cracking of the films, probably due to dehydration of the film and/or mismatch of the linear thermal expansion coefficients for the coatings and substrate. For example, stainless steel, a common substrate used for ceria deposition, has a linear thermal expansion coefficient of ~12.5 x 10^{-6} K^{-1}. For ceria, the linear thermal expansion coefficient has been reported to range from 9 to 18 x 10^{-6} K^{-1} at 298 K [66-69]. In addition, α increased as the oxygen vacancies increased for ceria, indicating that the +3/+4 ratio of cerium in the coatings is important. It is reasonable to assume that the thermal expansion coefficient values for thin coatings or nanocrystalline films will be different than that measured for bulk cerium oxide. This cracking or "stain-glass" effect that occurs for deposition of CeO_2 can be seen in Figure 2. Zhitomirsky added polymers (PVB or PVP) into the deposition solution, which were electrochemically intercalated into the deposit, so that the resultant films exhibited better adherence and crack-proof properties [63, 70]. Switzer took a different approach, in which he used anodic deposition at different applied voltages to directly oxidize Ce(III) to Ce(IV) and obtained crack free films [25]. A XANE study on electrodeposited cerium oxide thin films revealed that anodic deposition led to higher percentage of Ce(IV) species while cathodic base generation method led to the formation of high percentage of Ce(III) species in the composition [71]. In fact, no matter what electrode-position method is used, the coatings obtained typically have a mixed stoichiometry of CeO_{2-x}. Much of the work for deposition of cerium oxide has been done using the base generation method; however several researchers have studied the deposition using direct oxidation of Ce(III) to Ce(IV) to produce the films [25, 27, 28, 72].

Direct anodic deposition of CeO_2 as a film is difficult in aqueous solutions. A simplified Pourbaix diagram, as shown in Figure 3, can help elucidate the different species that are stable at various pHs and voltages [34]. The dotted lines frame the boundaries of oxidation and reduction for water. At pHs below 7, Ce^{3+} ions are stable between the reduction and oxidation limits of the electrolyte; however, as the pH increases above 7, $Ce(OH)_3$ precipitates.

Golden et al. proposed a deposition route in which the Ce^{3+} ion in solution was first stabilized using a ligand [27, 28]. Several weakly to strongly bound cerium complexes were studied for the direct anodic deposition of CeO_2. The deposition proceeded best when a ligand such as acetate or lactate was complexed with cerium in solution. The deposition was found to be pH and temperature dependent. Figure 4 shows the x-ray diffraction patterns for films deposited at different pHs. As seen from the XRD pattern, for a solution pH between 7 and 9, the deposited CeO_2 film exhibits a preferred (111) orientation, but at a pH of 9 to 11, the CeO_2 films exhibit a random orientation. At solution pHs higher than 11, no CeO_2 deposits on the electrode surface, although CeO_2 powder (confirmed by XRD) is generated and settles at the bottom of the reaction cell. Golden et al. found that the preferred oriented CeO_2 films could be obtained by tailoring the deposition conditions. The optimized deposition parameters included anodic deposition at current densities lower than -0.06 mA/cm^2 and temperatures higher than 50 °C [1].
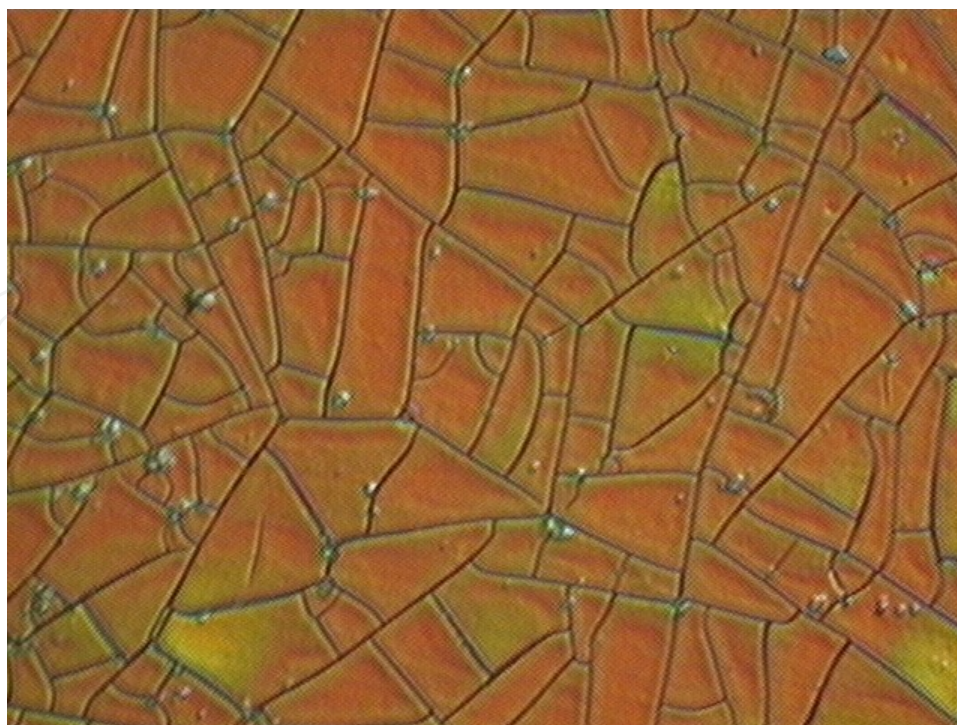
Figure 2. Optical Micrograph of an electrodeposited cerium oxide film on stainless steel. 800x magnification. (from T. Golden).
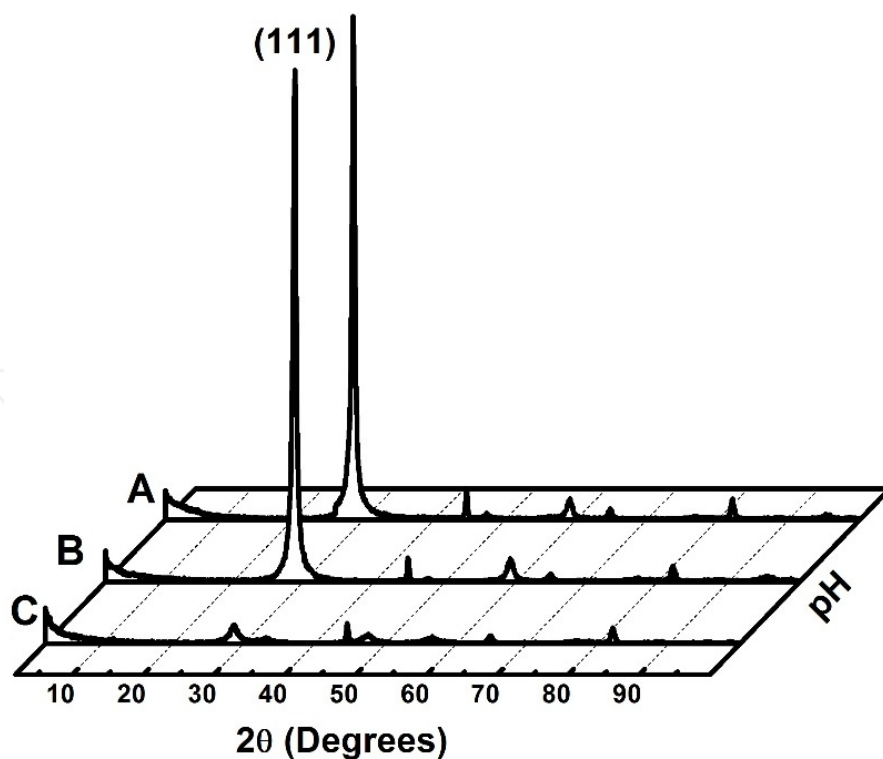

Figure 4. X-ray diffraction patterns of cerium oxide films deposited at a pH of (A) 7.5, (B) 8.5 and (C) 10.5. Deposition temperature, 70 ºC; j_{anodic} = -0.06 mA/cm². Y-axis represents x-ray intensity in cps.

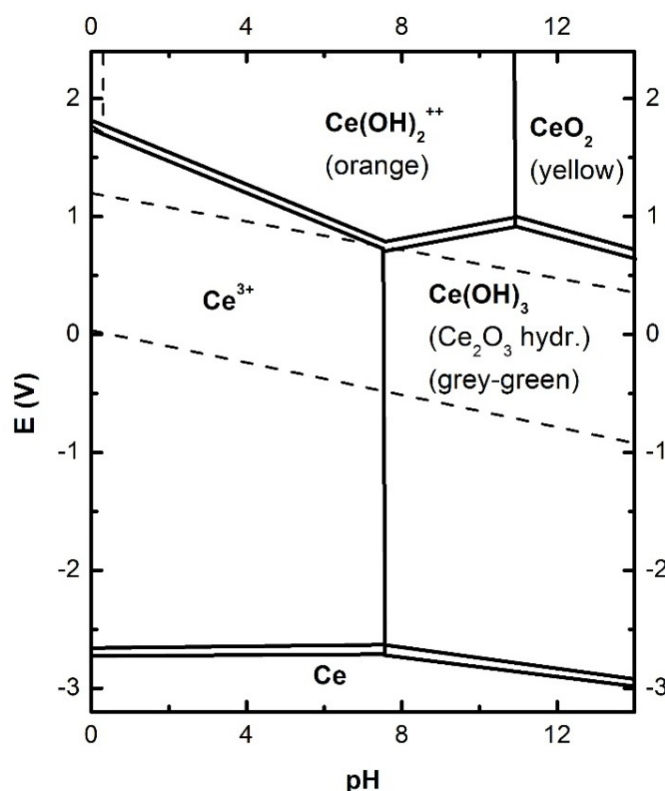**Figure 3.** Simplified Pourbaix diagram for the Ce system in aqueous solution.

The electrodeposition of cerium oxide has an approximate linear relationship with fixed current density and deposition time up to a point. Typically, the faradaic yield drops off 35% after a certain film thickness due to the insulating quality of the cerium oxide coating [73]. After long periods of deposition time (~24 hrs), the current becomes negligible. [27, 28].
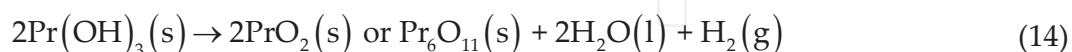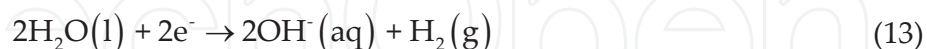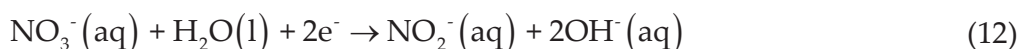
Cerium oxide has been deposited from electrolytic solution containing either cerium nitrate or cerium chloride salts. Using chloride salts poses a problem, in that the deposits tend to be amorphous and incorporate chloride ions into the films except under certain conditions. Creus et al. found that to deposit using cerium chloride salts required either an addition of H_2O_2 to the aqueous electrolyte solution or use of a mixed water–ethyl alcohol solution [74]. Others also found that the base generation method could be used for the deposition from chloride salts when the plating solution contained a mixture of water and ethanol [70, 75, 76].

A major thrust in recent years has been to electrodeposit cerium oxide onto various substrates for corrosion protection. Successful deposition of cerium oxide has been accomplished on surfaces such steels [77-79], zinc [15, 80], aluminum [81], and nickel superalloys [82, 83]. Linear polarization and tafel analysis were applied to test the corrosion protection effect of the as-deposited cerium oxide–oriented films [1]. The corrosion current decreased from 7.94×10^{-9} for the substrate to 7.59×10^{-10} A•cm^{-2} for the CeO_2 film coated substrate in a 0.1 M NaCl solution. Film coated substrate in a 0.1 M NaCl increased from 2.63×10^6 for the substrate to 6.69×10^7 Ω•cm^2 for the CeO_2 film showing increased corrosion protection for the coating.

5. Electrochemical synthesis of praseodymium oxides

Praseodymium oxide is a versatile and useful material, which is made up of a series of oxide compounds with the general formula Pr_nO_{2n-2} (n=4, 5, 6, 7, 8, 9, 10, 12) [84-86]. Pr_2O_3 has a hexagonal structure and belongs to the A-type rare earth structure, while, PrO_2 and Pr_6O_{11} have a fluorite structure (similar to CeO_2) where the metals are eight-coordinate. The mixed valence states in praseodymium oxide compounds make them useful materials with several important applications. Two areas of interest for praseodymium oxide films include the use of this material as an ethanol sensor and as a catalyst. [87-90]. Tsang et al. found that Pr_6O_{11} could detect ethanol in air and the optimal sensitivity (100%) was obtained at about 250 °C – 300 °C [87]. The Pr_6O_{11} sensors gave a linear response to ethanol concentrations in the range of 200–8000 ppm. Praseodymium oxide is a promising candidate to substitute silicon dioxide as a high-K dielectric, with a dielectric constant up to 10 times higher than SiO_2 (dielectric constant is around 30) and very low leakage currents. Among the different compositions of praseodymium oxide, Pr_6O_{11} has the highest K value and Pr_2O_3 is a good dielectric [91-93]. Praseodymium oxide films can be formed by several different methods including molecular beam epitaxy, pulsed-laser deposition (PLD), sputtering, electrocrystallization of molten salts, chemical vapor deposition (CVD), and spin coating [92, 94-99].

However, the literature for the electrochemical deposition of praseodymium oxide is quite sparse. There are only a couple of references using electrodeposition and even in these the initial deposition component is praseodymium hydroxide, which is converted to Pr_6O_{11} or PrO_2 by sintering [100, 101]. In both instances, $Pr(NO_3)_3$ and H_2O_2 were used as electrolyte and the deposition occurred by the base generation method. The reactions are [101]:

$$H_2O_2(aq) + 2e^- \rightarrow 2OH^-(aq) \tag{11}$$

$$NO_3^-(aq) + H_2O(l) + 2e^- \rightarrow NO_2^-(aq) + 2OH^-(aq) \tag{12}$$

$$2H_2O(l) + 2e^- \rightarrow 2OH^-(aq) + H_2(g) \tag{13}$$

$$2Pr(OH)_3(s) \rightarrow 2PrO_2(s) \text{ or } Pr_6O_{11}(s) + 2H_2O(l) + H_2(g) \tag{14}$$

where the electrochemical generation of hydroxide ions increases the pH at the electrode surface and causes formation of Pr hydroxide on the surface. After deposition, the film is dried and sintered to produce Pr oxide.

Shrestha et al. electrodeposited an ultrathin layer of praseodymium hydroxide on ITO by applying a cathodic sweeping voltage followed by thermal annealing at 500°C for 1 h [100]. The predominant phase of the annealed film was Pr_6O_{11}. The XRD pattern of the deposit was

indexed as Pr_6O_{11} (JCPDS 06-0329). The SEM showed the surface covered with small and uniform globular shaped Pr_6O_{11} particles. The deposited particles did not seem to undergo aggregation into larger islands on the ITO surface, suggesting that the colloidal particles once formed near the cathode quickly accumulated on the ITO surface in the short electrodeposition time. The surface coverage increased with the number of electrodeposition cycles.

Golden et al. studied using both potentiostatic and galvanostatic control for the cathodic deposition method to produce Pr oxide films. For the potentiostatic method, a potential from -1.0 V to -1.3 V was maintained while for the galvanostatic method, the deposition current density was set at 0.8 mA/cm^2. The electrolyte solution contained praseodymium nitrate, ammonium nitrate, and potassium chloride. A simplified Pourbaix diagram is shown in Figure 5. Within the aqueous region, at acidic pHs the Pr^{3+} ion is stable and at basic pHs the Pr hydroxide is stable. PrO_2 is stable at pH above 8, but is at an overpotential above O_2 evolution in the aqueous solution. Therefore, increasing the local pH at the electrode surface by generating base is likely to produce Pr hydroxide nuclei for deposition.
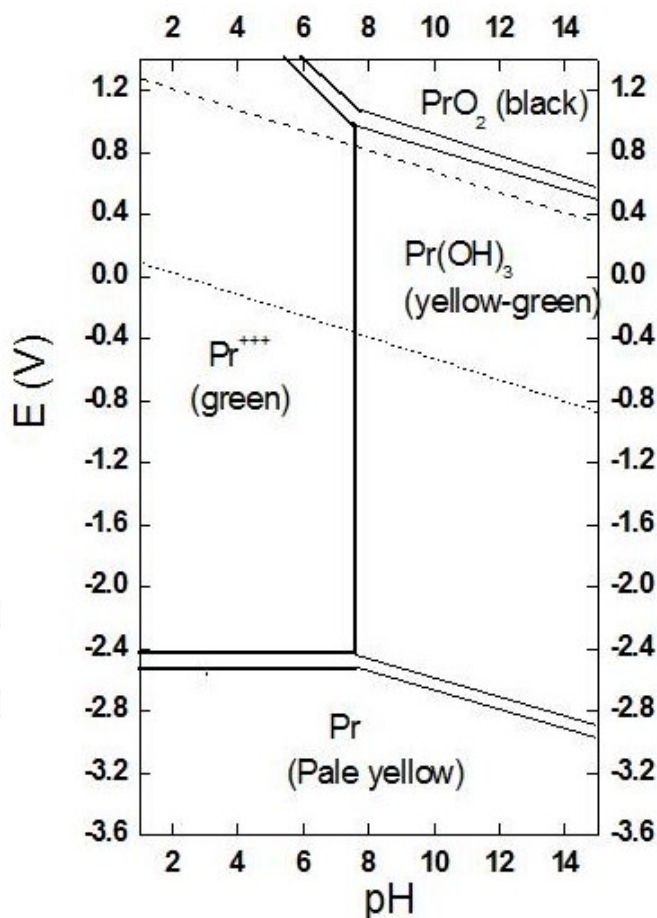

Figure 5. Simplified Pourbaix diagram for the Pr system in aqueous solution.

The XRD pattern for the as deposited film on a stainless steel substrate is shown in Figure 6. Both potentiostatic and galvanostatic methods gave similar results. The XRD pattern matches

the reflections for Pr(OH)$_3$ with some Pr(NO$_3$)$_3$ contamination. Pr compounds have a light green color when the valence of Pr is +3, or dark brown/black color when the valence is +4. Since the film on the stainless steel substrate is a light green color, the valence state of Pr in the film is probably closer to +3. The newly deposited films were sintered at 600 °C, and the film color turned black. Figure 7 is the XRD pattern of a sintered electrodeposited film. The XRD pattern matches a random orientation of Pr$_6$O$_{11}$ face-centered cubic (fcc) structure (PDF #42-1121). Table 1 shows a comparison of the experimental data to the ICDD database for Pr$_6$O$_{11}$.
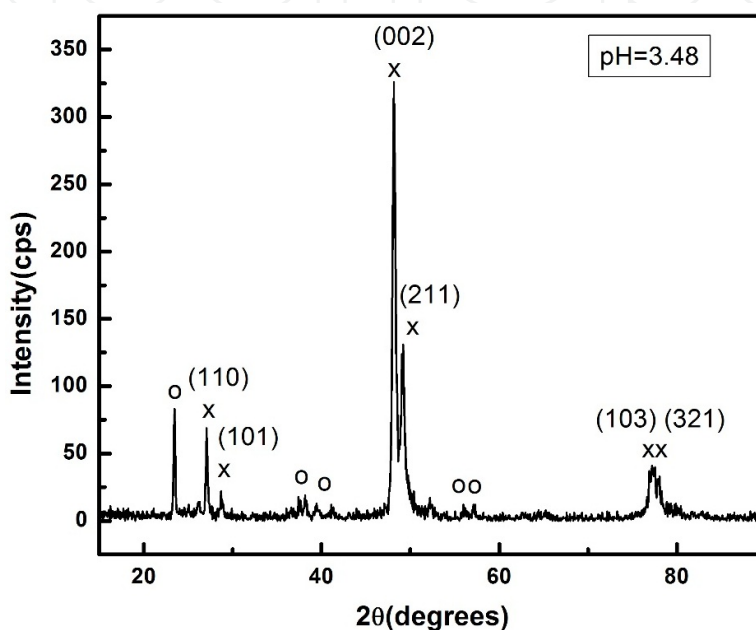

Figure 6. XRD pattern of the electrodeposited film on a stainless steel substrate using galvanostatic method with applied current density of 0.8 mA/cm^2, electrolyte solution composed of 0.1 M NH$_4$NO$_3$ and 0.1 M Pr(NO$_3$)$_3$, pH=3.48).

The crystallite size and strain of the praseodymium oxide films were also calculated from the XRD data by examining the peak position and peak broadening of the reflections. The broadening of the peaks arises from three areas: instrumental broadening, crystallite size, and lattice strain. Contributions from these three factors can be determined by the Williamson–Hall method when at least 3 or 4 peaks exist in a XRD pattern [102]. Separation of the peak broadening due to crystallite size and lattice strain can be obtained by plotting B$_r$cosθ versus sinθ, where the crystallite size is calculated from the y-intercept and strain from the slope. The calculated crystallite size ranged from 20 to 40 nm for the electrodeposited Pr oxide films.

The oxidation state of Pr in sintered praseodymium oxide films can be studied using XPS. The core-level binding energies for praseodymium oxide and the exact position of each peak from XPS are listed into Table 2. Figure 8 is the high resolution XPS spectra of the Pr 3d core level showing the 3d5/2 and 3d3/2 signals separated by 20.2 eV, with the peak positions at 933.3 eV and 953.5 eV, respectively. A strong shoulder can be seen on the lower BE sides of the Pr 3d5/2 and Pr 3d3/2 peaks, with comparable intensity and a distance between around 4.5 and 4.3 eV,
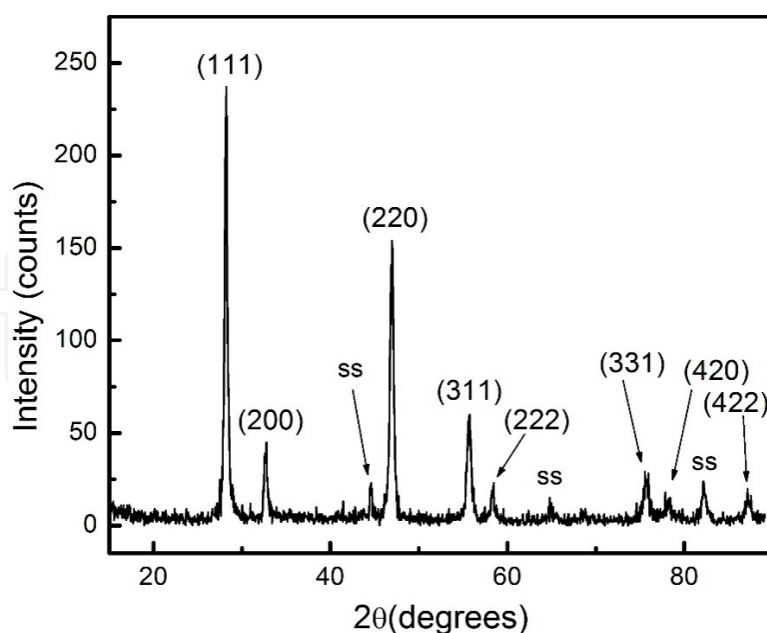
Figure 7. XRD pattern of praseodymium oxide film obtained by sintering the deposited film at 600 °C for 1 h.

hkl	Experimental 2θ(°)	I/I₀	PDF #42-1121 θ(°)	I/I₀
111	28.238	100	28.249	100
200	32.741	18	32.739	28
220	46.951	65	46.993	30
311	55.743	24	55.706	24
222	58.436	8	58.424	4
400	-	-	68.588	3
331	75.557	10	75.753	5
420	78.065	6	78.083	4
422	87.255	7	87.265	4

Table 1. Comparison of XRD data of the sintered electrodeposited film and PDF card. (Golden et al.).

this is consistent with results in literature for praseodymium [103, 104]. The XPS spectra of polycrystalline powders of Pr_2O_3, PrO_2 and Pr_6O_{11} all have an energy separation of the Pr 3d3/2 and Pr 3d5/2 core levels in the range of 17.5–23.0 eV. In addition, the Pr 3d5/2 core level spectra of these praseodymium oxides exhibit a shoulder at 4–4.5 eV on the lower binding energy side of the metal main peak. The relative intensities of the Pr 3d main peak and satellite peak vary with the Pr(III)/Pr(IV) ratio [105]. Specifically, the main peak intensity increases as the relative content of Pr(III) increases whereas the satellite peak intensity decreases. Therefore, the variation of relative intensities of the main and satellite peaks can be used to examine the change in Pr valence. The Pr 3d XPS spectra of Pr_2O_3 and PrO_2 are almost identical in most

respects, such as the shape of the peak and the overall fine structure. The main and satellite peaks for Pr_6O_{11} are situated between PrO_2 and Pr_2O_3. The Pr 3d5/2 binding energy is 935.0 eV for Pr(IV) and 932.9 eV for Pr(III). Our experimental results are 933.3 eV for Pr 3d5/2, which is an indication of a Pr +3/+4 mixture such as in Pr_6O_{11}. By curve fitting the Pr 3d XPS spectrum and determining the areas of the fitted peaks, a non-stoichiometric ratio is determined as $PrO_{1.80}$, an indication of the mixed valence state of Pr(III) and Pr(IV) (Table 3).

Oxide	Pr 5p	Pr 5s	Pr 4d	Pr 4p	Pr 4s	Pr $3d_{5/2}$	Pr $3d_{3/2}$	O1s
Peak position (eV)	20.08	36.8	116.2	217.2	304.7	933.3	954.7	530.3

Table 2. Core-level binding energies for sintered electrodeposited praseodymium oxide measured by XPS.
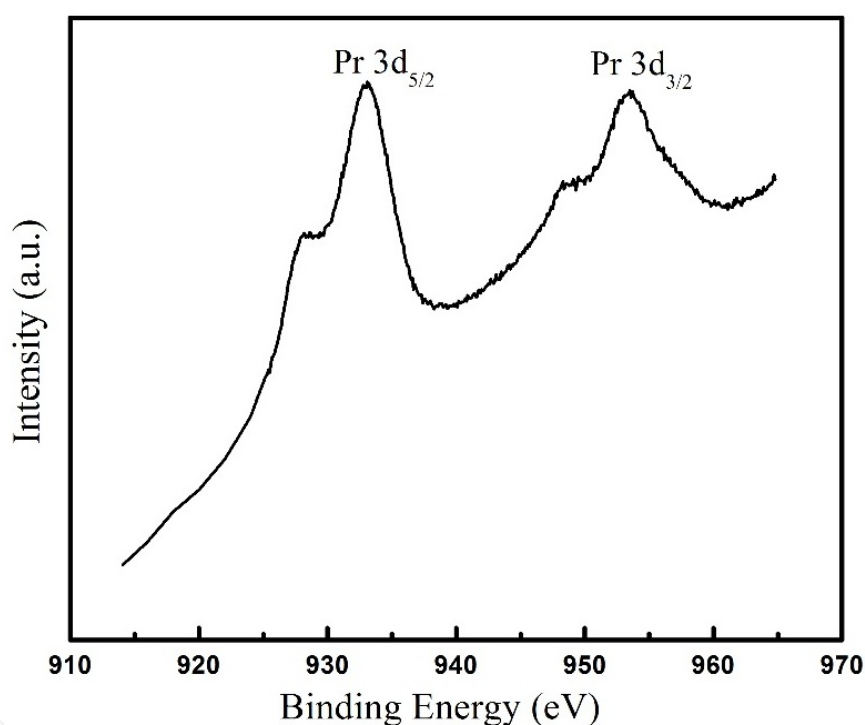

Figure 8. High-resolution XPS spectra of Pr 3d core level showing the spin-orbit splitting of the 3d level.

The pH effect was also studied as one of the parameters for the electrodeposition of the Pr oxide films. When the pH value of the electrolyte solution was below 7, films could be electrodeposited onto the substrate; however, powders only formed in the solution when the pH was above 7, due to bulk formation of $Pr(OH)_3$. XRD of the electrodeposited films showed that intensities of the reflections belonging to $Pr(OH)_3$, such as (110), (101), (103), (321), and (220), increased with increasing pH (up to pH 7) of the electrolyte, and the intensities of the peaks due to $Pr(NO_3)_3$ decreased with increasing pH.

The morphology of the praseodymium oxide film is interesting and is shown in Figure 9. Before sintering, the films appeared smooth and continuous, but after sintering, cracks appeared in

the films (similar to CeO_2 films) due to shrinkage and mismatch between the film and substrate. However, at higher magnification in the SEM images, the Pr oxide is distributed as platelets across the surface and the film has a high surface area. This may be beneficial in catalysis.

Peak #	Praseodymium contribution	Peak position (eV)	Area	% Area
m_1	Pr(III)	927.408	171980	9.7440
m_2	Pr(IV)	928.837	207250	11.74221
s_2	Pr(IV)	932.384	423730	24.0079
s_1	Pr(III)	934.128	261960	14.8424
m_1'	Pr(III)	947.820	132190	7.48986
m_2'	Pr(IV)	948.956	82829.93	4.69302
s_2'	Pr(IV)	953.220	363640	20.6030
s_1'	Pr(III)	956.640	121380	6.8773
Total			1764960	100
Pr(III)			687510	38.9537
Pr(IV)/Pr(III)				1.567

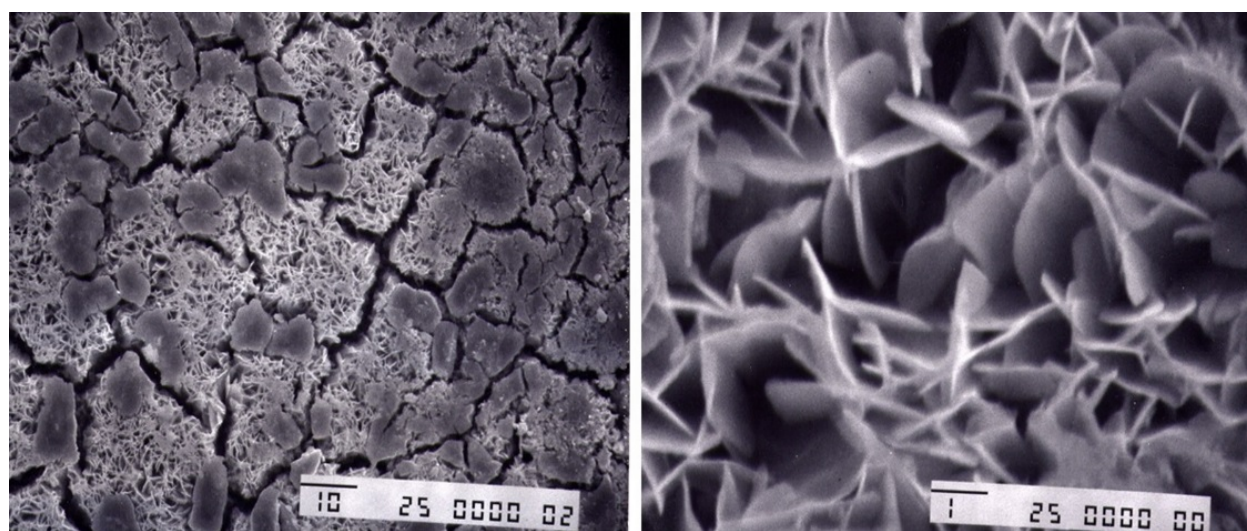**Table 3.** Peak list of Pr 3d and calculation of Pr valence.

Figure 9. SEM images of Pr_6O_{11} film obtained by cathodic electrodeposition on stainless steel in an electrolyte system composed of 0.1M $Pr(NO_3)_3$ and 0.1M NH_4NO_3 solution, j = 0.8 mA/cm², T= 25 °C, and after sintering at 600 °C for 1 h; (left) magnification 1000. (T. Golden); (right) magnification 10000.

In conclusion, Pr_6O_{11} films were successfully obtained on stainless steel substrates (Golden et al.) using the base generation method and then sintered at 600 °C. X-ray diffraction

showed the films matched the Pr_6O_{11} fluorite structure and the crystallite size was calculated as 20 to 40 nm. Scanning electron microscopy was utilized to study the surface texture and microstructure of deposits. As-deposited films had uniform morphology but sintering caused cracking of the films. SEM showed interesting surface texture and platelet structure for the deposits. The oxidation state of Pr oxide was determined by XPS and revealed that the praseodymium oxide was non-stoichiometric with the oxidation state of Pr between +3 and +4.

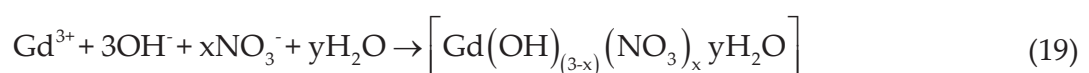# 6. Electrochemical synthesis of other rare earth oxides

The remaining literature for electrodeposition of pure rare earth oxides is sparse. Most of the research is on doping of CeO_2 with another rare earth oxide (i.e., PrO_2, Sm_2O_3, Gd_2O_3, and Tb_2O_3) to increase the oxygen vacancies, ionic conductivity, or catalytic activity [106-109]. However, there are a few reports of individual REO coatings prepared by electrodeposition using the base generation method. Lair et al. prepared Sm_2O_3 by electrodepositing $Sm(OH)_3$ from a nitrate solution and then sintering at 600 °C for 1 h [110]. The as-deposited Sm-based films were thick and adherent to the substrate even though cracking was observed in the film. Raman spectra of the as-deposited films had peaks at 1054 and 741 cm^{-1} attributed to the internal vibration modes of nitrate ions. Both nitrate-related peaks greatly diminished after annealing and major peaks for Sm_2O_3 increased in the spectrum.

Other researchers prepared Gd_2O_3 by electrodepositing $Gd(OH)_3$ from a nitrate solution and then sintering at 700 °C for 3 h [111, 112]. The authors used a cathodic pulse current method where $t_{on} = 10$ ms and $t_{off} = 10$ ms. The deposition mechanism was still a base generation method:

Electrochemical step:

$$NO_3^- + H_2O + 2e^- \rightarrow NO_2^- + 2OH^- \tag{15}$$

$$O_2 + 2H_2O + 4e^- \rightarrow 4OH^- \tag{16}$$

$$2H_2O + 2e^- \rightarrow H_2 + 2OH^- \tag{17}$$

Chemical step:

$$Gd^{3+} + 3OH^- + yH_2O \rightarrow \left[Gd(OH)_3 \, yH_2O \right] \tag{18}$$

$$Gd^{3+} + 3OH^- + xNO_3^- + yH_2O \rightarrow \left[Gd(OH)_{(3-x)} (NO_3)_x \, yH_2O \right] \tag{19}$$

The reduction of nitrate ions and water in the electrochemical step causes the electrogeneration of base at the cathode surface due to the increase of local pH, which leads to the formation of gadolinium hydroxide deposit on the electrode. Analysis of the films showed a high nitrogen content indicating nitrate ions had been intercalated into the deposit during electrodeposition. SEM images of the sintered coatings did show formed nanorods ~20–30 nm in diameter and up to 1 μm in length.

Lu et al. electrodeposited TbO_{2-x} coatings onto copper substrates from a nitrate solution using the base generation method [113]. SEM images of the electrodeposited TbO_{2-x} samples showed flower-like structures made up of numerous leaf-like nanosheets, in which the leaf-shaped nanosheets were approximately 100 nm in thickness and 1 μm in width. The crystal structure was analyzed by powder XRD. The values of the lattice constant were close to those of $TbO_{1.75}$.

7. Conclusion

The electrodeposition of rare earth oxides onto various substrates can be accomplished by two different electrochemical mechanisms: cathodic electrogeneration of base method or direct anodic deposition. The majority of the literature for REO electrodeposition covers CeO_2 or REO-doped CeO_2. A variety of morphologies has been obtained for the REOs films, such as nanocrystalline films, nanorods, nanotubes, nanosheets, as well as flower-like and coral-like nanostructures. Some sections covered in detail include the direct electrodeposition of CeO_2 using a complexing ligand to stabilize the ceria ions in solution and the cathodic deposition of Pr_6O_{11}.

Author details

Teresa D. Golden[1*], Yajuan Shang[2], Qi Wang[3] and Ting Zhou[1]

*Address all correspondence to: tgolden@unt.edu

1 University of North Texas, Department of Chemistry, Denton, TX, USA

2 Eli Lilly & Company, Indianapolis, USA

3 Yeshiva University, Department of Physics, New York, USA

References

[1] Wang AQ, Golden TD. Electrodeposition of oriented cerium oxide films. Int. J. Electrochem. 2013;482187:1-10. DOI: 10.1155/2013/482187.

[2] Wang AQ, D'Souza NA, Golden TD. Electrosynthesis of nanocrystalline cerium oxide/layered silicate powders. J. Mater. Chem. 2006;16:481-488. DOI: 10.1039/B506976A.

[3] Wang Q, D'Souza NA, Golden TD. Ceramic montmorillonite nanocomposites by electrochemical synthesis. Appl. Clay Sci. 2008;42:310-317. DOI: 10.1016/j.clay.2008.02.004.

[4] Duran P, Recio P, Jurado JR, Pascual C, Moure C. Preparation, sintering, and properties of translucent erbium oxide (Er_2O_3)-doped tetragonal zirconia. J. Am. Ceram. Soc. 1989;72:2088-2093. DOI: 10.1111/j.1151-2916.1989.tb06036.x.

[5] Erbe EM, Day DE. Properties of Sm_2O_3-Al_2O_3-SiO_2 glasses for in vivo applications. J. Am. Ceram. Soc. 1990;73:2708-2713. DOI: 10.1111/j.1151-2916.1990.tb06750.x.

[6] Zhang P, Lu Z, Yuan Q, Hou Q, Golden TD, Ren X, Weng L, Wang H. A novel composite phosphor via one-pot synthesis: Single matrix with controllable luminescence. Mater. Chem. Phys. 2012;134:1190-1196. DOI: 10.1016/j.matchemphys.2012.04.020.

[7] Schubert EF, Kim JK. Solid-state light sources getting smart. Science. 2005;308:1274-1278. DOI: 10.1126/science.1108712.

[8] Shelef M, McCabe RW. Twenty-five years after introduction of automotive catalysts: what next? Catal. Today. 2000;62:35-50. DOI: 10.1016/S0920-5861(00)00407-7.

[9] Niu X, Du W, Du W. Preparation, characterization and gas-sensing properties of rare earth mixed oxides. Sensor Actuat. B-Chem. 2004;99:399-404. DOI: 10.1016/j.snb.2003.12.006.

[10] Niu X, Zhong H, Wang X, Jiang K. Sensing properties of rare earth oxide doped In_2O_3 by a sol-gel method. Sensor Actuat. B-Chem. 2006;115:434-438. DOI: 10.1016/j.snb.2005.10.004.

[11] Murray EP, Tsai T, Barnett SA. A direct-methane fuel cell with a ceria-based anode. Nature. 1999;400:649-651. DOI: 10.1038/23220.

[12] Singhal, SC. Advances in solid oxide fuel cell technology. Solid State Ionics. 2000;135:305-313. DOI: 10.1016/S0167-2738(00)00452-5.

[13] Monte RD, Kaspar J. Nanostructures CeO_2-ZnO_2 mixed oxides. J. Mater. Chem. 2005;15:633-648. DOI: 10.1039/b414244f.

[14] Colussi S, De Leitenburg C, Dolcetti G, Trovarelli A. The role of rare earth oxides as promoters and stabilizers in combustion catalysts. J. Alloys Compd. 2004;374:387-392. DOI: 10.1016/j.jallcom.2003.11.028.

[15] Hamlaouri Y, Remazeilles C, Bordes M, Tifouti L, Pedraza F. Electrodeposition of ceria-based layers on zinc electroplated steel. Corr. Sci. 2010;52:1020-1025. DOI: 10.1016/j.corsci.2009.11.027.

[16] Huang X, Li N, Wang H, Sun H, Sun S, Zhang J. Electrodeposited cerium film as chromate replacement for tinplate. Thin Solid Films. 2008;516:1037-1043. DOI: 10.1016/j.tsf.2007.08.044.

[17] Stoyanova E, Stoychev D. in: Hong S. Corrosion behavior of stainless steels modified by cerium oxides layers. Handbook of Corrosion Resistance. Croatia: InTech; 2012. 239 p. DOI: 10.5772/33382.

[18] Rudd AL, Breslin CB, Mansfeld F. The corrosion protection afforded by rare earth conversion coatings applied to magnesium. Corros. Sci. 2000;42:275-288. DOI: 10.1016/S0010-938X(99)00076-1.

[19] Liu T, Zhang Y, Shao H, Li X. Synthesis and characteristics of Sm_2O_3 and Nd_2O_3 nanoparticles. Langmuir. 2003;19:7569-7572. DOI: 10.1021/la034350l.

[20] Yu X, Li F, Ye X, Xin X, Xue Z. Synthesis of cerium(IV) oxide ultrafine particles by solid-state reactions. J. Am. Ceram. Soc. 2000;83:964-966. DOI: 10.1111/j. 1151-2916.2000.tb01306.x.

[21] Ozer N. Optical properties and electrochromic characterization of sol-gel deposited ceria films. Sol. Energy Mater. Sol. Cells. 2001;68:391-400. DOI: 10.1016/ S0927-0248(00)00371-8.

[22] Mikhelashvili V, Eisenstein G, Edelmann F. Characteristics of electron-beam-gun-evaporated Er_2O_3 thin films as gate dielectrics for silicon. J. Appl. Phys. 2001;90:5447-5449. DOI: 10.1063/1.1413239.

[23] Jones L, Kumar D, Singh RK, Holloway PH. Luminescence of pulsed laser deposited Eu doped yttrium oxide films. Appl. Phys. Lett. 1997;71:404-406. DOI: S0003-6951(97)03027-1.

[24] Kale SS, Jadhav KR, Patil PS. Characterizations of spray-deposited lanthanum oxide (La_2O_3) thin films. Mater. Lett. 2005;59:3007-3009. DOI: 10.1016/j.matlet.2005.02.091.

[25] Kulp EA, Limmer SJ, Bohannan EW, Switzer JA. Electrodeposition of nanometer-thick ceria films by oxidation of cerium (III)-acetate. Solid State Ionics. 2007;178:749-757. DOI: 10.1016/j.ssi.2007.03.012.

[26] Zhou Y, Phillips RJ, Switzer JA. Electrochemical synthesis and sintering of nanocrystalline cerium (IV) oxide powders. J. Am. Ceram. Soc. 1995;78:981-985. DOI: 10.1111/j. 1151-2916.1995.tb08425.x.

[27] Wang Q, Golden TD. Anodic deposition of cerium oxide: I. Formation of crystalline thin films. J. Electrochem. Soc. 2003;150:C616-C620. DOI: 10.1149/1.1596164.

[28] Golden TD, Wang Q. Anodic deposition of cerium oxide thin films: II. Mechanism studies. J. Electrochem. Soc. 2003;150:C621-C624. DOI: 10.1149/1.1596165.

[29] Conrad HA, Corbett JR, Golden TD. Electrochemical deposition of γ-phase zinc-nickel alloys from alkaline solution. J. Electrochem. Soc. 2012;159:C29-C32. DOI: 10.1149/2.027201jes.

[30] Ahmad YH, Mohamed AMA. Electrodeposition of nanostructured nickel-ceramic composite coatings: a review. Int. J. Electrochem. Sci. 2014;9:1942-1963. ISSN: 1452-3981.

[31] Ahmad YH, Tientong J, D'Souza N, Mohamed AMA, Golden TD. Characterization and corrosion resistance of electrodeposited Ni-Mo-silicate platelet nanocomposite coatings. Surf. Coat. Technol. 2014;259:517-525. DOI: 10.1016/j.surfcoat.2014.10.036.

[32] Switzer JA. Electrochemical synthesis of ceramic films and powders. Am. Ceramic Soc. Bull. 1987;66:1521-1524. ISSN: 0002-7812.

[33] Therese GHA, Kamath, PV. Electrochemical synthesis of metal oxides and hydroxides. Chem. Mater. 2000;12:1195-1204. DOI: 10.1021/cm990447a.

[34] Pourbaix M. Handbook of Atlas of Electrochemical Equilibria in Aqueous Solutions. Houston: NACE; 1974. 644 p. DOI: 10.1016/0022-0728(67)80059-7.

[35] Mao G, Zhang H, Lia H. Selective Synthesis of morphology and species controlled La_2O_3:Eu^{3+} and $La_2O_2CO_3$:Eu^{3+} phosphors by hydrothermal method. J. Electrochem. Soc. 2012;159:J48-J53. DOI: 10.1149/2.031203jes.

[36] Muttay EP, Tsai T, Barnett SA. A direct-methane fuel cell with a ceria-based anode. Nature. 1999;400:649-651. DOI: 10.1038/23220.

[37] Andriamasinoro D, Kieffer R, Kiennemann A, Poix P. Preparation of stabilized copper-rare earth oxide catalysts for the synthesis of methanol from syngas. Appl. Catal. 1993;106:201-212. DOI: 10.1016/0926-860X(93)80178-S.

[38] Sun J, Qiu XP, Zhu WT. H_2 from steam reforming of ethanol at low temperature over Ni/Y_2O_3, Ni/La_2O_3 and Ni/Al_2O_3 catalysts for fuel-cell application. Int. J. Hydrogen Energy. 2005;30:437-445. DOI: 10.1016/j.ijhydene.2004.11.005.

[39] Gonzalez-Rovira L, Sanchez-Amaya JM, Lopez-Haro M, Hungria AB, Boukha Z, Bernal S, Botana FJ. Formation and characterization of nanotubes of La(OH)$_3$ obtained using porous alumina membranes. Nanotechnology. 2008;19:495305/1-495305/9. DOI: 10.1088/0957-4484/19/49/495305.

[40] Bocchetta P, Santamaria M, Di Quarto F. Template electrosynthesis of La(OH)$_3$ and Nd(OH)$_3$ nanowires using porous anodic alumina membranes. Electrochem. Commun. 2007;9:683-688. DOI: 10.1016/j.elecom.2006.10.053.

[41] Yao CZ, Wei BH, Ma HX, Gong QJ, Jing KW, Sun H, Meng LX. Facile fabrication of La(OH)$_3$ nanorod arrays and their application in wastewater treatment. Mater. Lett. 2011;65: 490-492. DOI: 10.1016/j.matlet.2010.10.065.

[42] Liu Z, Zheng D, Su Y. Facile and efficient electrochemical synthesis of lanthanum hydroxide nanospindles and nanorods. Electrochem. Solid-State Lett. 2010;13:E15-E18. DOI: 10.1149/1.3486446.

[43] Khosrow F, Aghazadeh M, Arhamib B. Facile synthesis of vertically aligned one-dimensional (1D) $La(OH)_3$ and La_2O_3 nanorods by pulse current deposition. J. Electrochem. Soc. 2013;160:D150-D155. DOI: 10.1149/2.050304jes.

[44] Aghazadeh M, Golikand AN, Ghaemi M, Yousefi T. A novel lanthanum hydroxide nanostructure prepared by cathodic electrodeposition. Mater. Lett. 2011;65:1466-1468. DOI: 10.1016/j.matlet.2011.02.039.

[45] Aghazadeh M, Golikand AN, Ghaemi M, Yousefi T. La_2O_3 nanoplates prepared by heat-treatment of electrochemically grown $La(OH)_3$ nanocapsules from nitrate medium. J. Electrochem. Soc. 2011;158:E136-E141. DOI: 10.1149/2.057112jes.

[46] Trovareli A. Catalytic properties of ceria and CeO_2-containing materials. Cat. Rev. - Sci. Eng. 1996;38:439-520. DOI: 10.1080/01614949608006464.

[47] Trovarelli A, Boaro M, Rocchini E, De Leitenburg C, Dolcetti G. Some recent developments in the characterization of ceria-based catalysts. J. Alloys Compd. 2001;323-324:584-591. DOI: 10.1016/S0925-8388(01)01181-1.

[48] Chiang YM, Lavik EB, Blom DA. Defect thermodynamics and electrical properties of nanocrystalline oxides: Pure and doped CeO_2. Nanostruct. Mater. 1997;9:633-642. DOI: 10.1016/S0965-9773(97)00142-6.

[49] Tschope A, Sommer E, Birringer R. Grain size-dependent electrical conductivity of polycrystalline cerium oxide I. Experiments. Solid State Ionics. 2001;139:255-265. DOI: 10.1016/S0167-2738(01)00678-6.

[50] Zhang Y, Anderson S, Muhammed M. Nanophase catalytic oxides: I. Synthesis of doped cerium oxides as oxygen storage promoters. Appl. Catal., B: Environ. 1995;6:325-337. DOI: 10.1016/0926-3373(95)00041-0.

[51] Tschope A, Liu W, Flytzani-Stephanopoulos M, Ying JY. Redox activity of nonstoichiometric cerium oxide-based nanocrystalline catalysts. J. Catal. 1995;157:42-50. DOI: 10.1006/jcat.1995.1266.

[52] Zhou Y, Rahaman MN. Effect of redox reaction on the sintering behavior of cerium oxide. Acta Mater. 1997;45:3635-3639. DOI: 10.1016/S1359-6454(97)00052-9.

[53] Kleinlogel C, Gaukler LJ. Sintering and properties of nanosized ceria solid solutions. Solid State Ionics. 2000;135:567-573. DOI: 10.1016/S0167-2738(00)00437-9.

[54] Arnott DR, Hinton BRW, Ryan NE, Cationic film-forming inhibitors for the protection of the AA 7075 aluminum alloy against corrosion in aqueous chloride solution. Corrosion (NACE). 1989;45:12-18. DOI: 10.5006/1.3577880.

[55] Crossland AC, Thompson GE, Skeldon P, Wood GC, Smith CJE, Habazaki H, Shimizu K. Anodic oxidation of Al-Ce alloys and inhibitive behavior of cerium species. Corros. Sci. 1998;40:871-885. DOI: 10.1016/S0010-938X(98)00007-9.

[56] Arenas MA, Conde A, De Damborenea J. Cerium: a suitable green corrosion inhibitor for tinplate. Corros. Sci. 2002;44:511-520. DOI: 10.1016/S0010-938X(01)00053-1.

[57] Zhou Y, Phillips RJ, Switzer JA. Electrochemical synthesis and sintering of nanocrystalline cerium(IV) oxide powders. J. Am. Ceram. Soc. 1995;78:981-985. DOI: 10.1111/j.1151-2916.1995.tb08425.x.

[58] Zhou Y, Switzer JA. Growth of cerium(IV) oxide films by the electrochemical generation of base method. J. Alloys Compd. 1996;237:1-5. DOI: 10.1016/0925-8388(95)02048-9.

[59] Aldykiewicz AJ, Davenport AJ, Isaacs HS. Studies of the formation of cerium-rich protective films using x-ray absorption near-edge spectroscopy and rotating disk electrode methods. J. Electrochem. Soc. 1996;143:147-153. DOI: 10.1149/1.1836400.

[60] Li F, Newman RC, Thompson GE. In situ atomic force microscopy studies of electrodeposition mechanism of cerium oxide films: nucleation and growth out of a gel mass precursor. Electrochim. Acta. 1997;42:2455-2464. DOI: 10.1016/S0013-4686(96)00433-1.

[61] Li F, Thompson GE, Newman RC. Force modulation atomic force microscopy: background, development and application to electrodeposited cerium oxide films. Appl. Surf. Sci. 1998;126:21-33. DOI: 10.1016/S0169-4332(97)00590-4.

[62] Li F, Thompson GE. In situ atomic force microscopy studies of the deposition of cerium oxide films on regularly corrugated surfaces. J. Electrochem. Soc. 1999;146:1809-1815. DOI: 10.1149/1.1391848.

[63] Zhitomirsky I, Petric A. Electrolytic and electrophoretic deposition of CeO_2 films. Mater. Lett. 1999;40:263-268. DOI: 10.1016/S0167-577X(99)00087-7.

[64] Zhitomirsky I. Cathodic electrosynthesis of titanium and ruthenium oxides. Mater. Lett. 1998;33:305-310. DOI: 10.1016/S0167-577X(97)00120-1.

[65] Zhitomirsky I, Petric A. Electrochemical deposition of ceria and doped ceria films. Ceram. Int. 2001;27:149-155. DOI: 10.1016/S0272-8842(00)00054-7.

[66] Hayashi H, Kanoh Ma, Quan CJ, Inaba H, Wang S, Dokiya M, Tagawa H. Thermal expansion of Gd-doped ceria and reduced ceria. Solid State Ionics. 2000;132:227-233. DOI: 10.1016/S0167-2738(00)00646-9.

[67] Touloukian YS, Kirby RK, Taylor RE, Lee TYR. in: Touloukian YS, Ho CY. Thermal expansion nonmetallic solids. Handbook of Thermophysical Properties of Matter. New York: Springer; 1977. 1810 p. DOI: 10.1007/978-1-4757-1631-3.

[68] Korner R, Ricken M, Noelting J, Riess I. Phase transformations in reduced ceria: determination by thermal expansion measurements. J. Solid State Chem. 1989;78:136-147. DOI: 10.1016/0022-4596(89)90137-0.

[69] Stecura S, Campbell WJ. Thermal expansion and phase inversion of rare-earth oxides. Bur. Mines Rept. Invest. 1961;5847:1-47. ISSN: 1066-5552.

[70] Yang L, Pang X, Fox-Rabinovich G, Veldhuis S, Zhitomirsky I. Electrodeposition of cerium oxide films and composites. Surf. Coat. Technol. 2011;206:1-7. DOI: 10.1016/j.surfcoat.2011.06.029.

[71] Balasubramanian M, Melendres CA, Mansour AN. An X-ray absorption study of the local structure of cerium in electrochemically deposited thin films. Thin Solid Films. 1999;347:178-183. DOI: 10.1016/S0040-6090(98)01754-4.

[72] Wang AQ, Punchaipetch P, Wallace RM, Golden TD. X-ray photoelectron spectroscopy study of electrodeposited nanostructured CeO_2 films. J. Vac. Sci. Technol. B. 2003;21:1169-1175. DOI: 10.1116/1.1577569.

[73] Arurault L, Monsang P, Salley J, Bes RS. Electrochemical preparation of adherent ceria coatings on ferritic stainless steel. Thin Solid Films. 2004;466:75-80. DOI: 10.1016/j.tsf.2004.02.039.

[74] Creus J, Brezault F, Rebere C, Gadouleau M. Synthesis and characterization of thin cerium oxide coatings elaborated by cathodic electrolytic deposition on steel substrate. Surf. Coat. Technol. 2006;200:4636-4645. DOI: 10.1016/j.surfcoat.2005.04.027.

[75] Stoyanova E, Guergova D, Stoychev D, Avramova I, Stefanov P. Passivity of OC404 steel modified electrochemically with CeO_2-Ce_2O_3 layers in sulfuric acid media. Electrochim. Acta. 2010;55:1725-1732. DOI: 10.1016/j.electacta.2009.10.057.

[76] Lu Y, Cai S, Liang Y, Bai C, Liu Z, Guo Y, Cai C. The mechanism of the nano-CeO_2 films deposition by electrochemistry method as coated conductor buffer layers. Physica C: Superconductivity and its Applications. 2015;512:1-5. DOI: 10.1016/j.physc.2015.02.038.

[77] Hamlaoui Y, Pedraza F, Remazeilles C, Cohendoz S, Rebere C, Tifouti L, Creus J. Cathodic electrodeposition of cerium-based oxides on carbon steel from concentrated cerium nitrate solutions: part I. Electrochemical and analytical characterization. Mater. Chem. Phys. 2009;113:650-657. DOI: 10.1016/j.matchemphys.2008.08.027.

[78] Hamlaoui Y, Tifouti L, Remazeilles C, Pedraza F. Cathodic electrodeposition of cerium based oxides on carbon steel from concentrated cerium nitrate. Part II: Influence of electrodeposition parameters and of the addition of PEG. Mater. Chem. Phys. 2010;120:172-180. DOI: 10.1016/j.matchemphys.2009.10.042.

[79] Hamlaoui Y, Pedraza F, Tifouti L. Investigation of electrodeposited cerium oxide based films on carbon steel and of the induced formation of carbonated green rusts. Corros. Sci. 2008;50:2182-2188. DOI: 10.1016/j.corsci.2008.05.017.

[80] Martinez L, Roman E, De Segovia JL, Poupard S, Creus J, Pedraza F. Surface study of cerium oxide based coatings obtained by cathodic electrodeposition on zinc. Appl. Surf. Sci. 2011;257:6202-6207. DOI: 10.1016/j.apsusc.2011.02.033.

[81] Zivkovic LjS, Popic JP, Jegdic BV, Dohcevic-Mitrovic Z, Bajat JB, Miskovic-Stankovic VB. Corrosion study of ceria coatings on AA6060 aluminum alloy obtained by cathodic electrodeposition: Effect of deposition potential. Surf. Coat. Technol. 2014;240:327-335. DOI: 10.1016/j.surfcoat.2013.12.048.

[82] Bouchaud B, Balmain J, Bonnet G, Pedraza F. Optimizing structural and compositional properties of electrodeposited ceria coatings for enhanced oxidation resistance of a nickel-based superalloy. Appl. Surf. Sci. 2013;268:218-224. DOI: 10.1016/j.apsusc.2012.12.065.

[83] Bouchaud B, Balmain J, Bonnet G, Pedraza F. Correlations between electrochemical mechanisms and growth of ceria based coatings onto nickel substrates. Electrochim. Acta. 2013;88:798-806. DOI: 10.1016/j.electacta.2012.10.112.

[84] Ferguson RE, Guth ED, Eyring L. Praseodymium oxides. I. Phase study by dissociation pressure measurements. J. Am. Chem. Soc. 1954;76:3890-3894. DOI: 10.1021/ja01644a006.

[85] Burnham DA, Eyring L. Phase transformations in the praseodymium oxide-oxygen system: high-temperature x-ray diffraction studies. J. Phys. Chem. 1968;72:4415-4424. DOI: 10.1021/j100859a010.

[86] Zhang J, Von-Dreele RB, Eyring L. Structures in the oxygen-deficient fluorite-related R_nO_{2n-2} homologous series: $Pr_{12}O_{22}$. J. Solid State Chem. 1996;122:53-58. DOI: 10.1006/jssc.1996.0081.

[87] Tsang SC, Bulpitt C. Rare earth oxide sensors for ethanol analysis. Sens. Actuators, B: Chemical. 1998;52:226-235. DOI: 10.1016/S0925-4005(98)00233-0.

[88] Hussein GAM. Rare earth metal oxides: formation, characterization and catalytic activity. Thermoanalytical and applied pyrolysis review. J. Anal. Appl. Pyrolysis. 1996;37:111-149. DOI: 10.1016/0165-2370(96)00941-2.

[89] Poirier MG, Breault R, Kaliaguine S, Adnot A. Oxidative coupling of methane over praseodymium oxide catalysts. Appl. Catal. 1991;71:103-122. DOI: 10.1016/0166-9834(91)85009-K.

[90] Du W, Xie Xi, Xu D, Huang C. Preparation and electrochemical characterization of $PtRuO_2$-$Ce_{0.5}Pr_{0.5}O_{2-\delta}$/C catalysts for methanol electrooxidation. Energy Fuels. 2008;22:3346-3350. DOI: 10.1021/ef800200u.

[91] Osten HJ, Liu JP, Müssig HJ, Zaumseil P. Epitaxial, high-k dielectrics on silicon: the example of praseodymium oxide. Microelectron. Reliab. 2001;41:991-994. DOI: 10.1016/S0026-2714(01)00054-3.

[92] Wolfframm D, Ratzke M, Kappa M, Montenegro MJ, Dobeli M, Lippert Th, Reif J. Pulsed laser deposition of thin Pr_xO_y films on Si(100). Mater. Sci. Eng., B. 2004;109:24-29. DOI: 10.1016/j.mseb.2003.10.022.

[93] Wu M, Alivov YI, Morkoc H. High-κ dielectrics and advanced channel concepts for Si MOSFET. J. Mater. Sci. - Mater. Electron. 2008;19:915-951. DOI: 10.1007/s10854-008-9713-2.

[94] Osten HJ, Liu JP, Mussig HJ. Band gap and band discontinuities at crystalline Pr_2O_3/Si(001) heterojunctions. Appl. Phys. Lett. 2002;80:297-299. DOI: 10.1063/1.1433909.

[95] Horio N, Hiramatsu M, Nawata M, Imaeda K, Torii T. Preparation of zinc oxide/metal oxide multilayered thin films for low-voltage varistors. Vacuum. 1998;51:719-722. DOI: 10.1016/S0042-207X(98)00293-0.

[96] Kaneko Y, Mori S, Yamanaka J. Synthesis of electrochromic praseodymium-doped vanadium oxide films by molten salt electrolysis. Solid State Ionics. 2002;151:35-39. DOI: 10.1016/S0167-2738(02)00601-X.

[97] Malchus M, Jansen M. Electrocrystallization of PrO_2 and TbO_{2-x} from alkali hydroxide melts and characterization of the fluorite-related TbO_{2-x}. Solid State Sci. 1998;2:65-70. DOI: 10.1016/S1293-2558(00)00111-4.

[98] Lo-Nigro R, Toro RG, Malandrino G, Fragala IL, Rossi P, Dapporto, P. Study of the thermal properties of Pr (III) precursors and their implementation in the MOCVD growth of praseodymium oxide films. J. Electrochem. Soc. 2004;151:F206-F213. DOI: 10.1149/1.1779336.

[99] Leach C, Freer R, Azough F, Ling Z. Direct observation of the barrier structure of a praseodymium-doped grain boundary in a zinc oxide bicrystal by charge collection microscopy. Interface Sci. 2000;8:141-146. DOI: 10.1023/A:1008772421392.

[100] Shrestha S, Marken F, Elliott J, Yeung CMY, Mills CE, Tsang SC. Electrochemical deposition of praseodymium oxide on tin-doped indium oxide as a thin sensing film. J. Electrochem. Soc. 2006;153:C517-C520. DOI: 10.1149/1.2198094.

[101] Sawangphruk M, Foord JS. Localized electrodeposition of praseodymium oxide on boron-doped diamond. Diamond Relat. Mater. 2010;19:885-888. DOI: 10.1016/j.diamond.2010.02.023.

[102] Cullity BD, Stock SR. Elements of X-ray Diffraction. 3rd ed. Prentice Hall; 2001, 664 p. ISBN-13: 978-0201610918.

[103] Sarma DD, Rao CNR. J. Electron. XPES studies of oxides of second- and third-row transition metals including rare earths. Spectrosc. Relat. Phenom. 1980;20:25-45. DOI: 10.1016/0368-2048(80)85003-1.

[104] Uwamino Y, Ishizuka T. X-ray photoelectron spectroscopy of rare-earth compounds. J. Electron. Spectrosc. Relat. Phenom. 1984;34:67-78. DOI: 10.1016/0368-2048(84)80060-2.

[105] Lei S, Yunsong H, Yunbo J, Xianming L, Guien Z, Yuheng Z. Study on the crystal and electronic structure of $Y_{1-x}Pr_xBa_2Cu_3O_{7-y}$ ceramics. J. Phys.: Condens. Matter. 1998;10:7015-7024. DOI: 10.1088/0953-8984/10/31/017.

[106] Rovira LG, Delgado JJ, ElAmrani K, Rio E, Chen X, Calvino JJ, Botana FJ. Synthesis of ceria-praseodimia nanotubes with high catalytic activity for CO oxidation. Catal. Today. 2012;180:167-173. DOI: 10.1016/j.cattod.2011.05.006.

[107] Zivkovic L, Lair V, Lupan O, Ringuede A. Effect of samarium addition and annealing on the properties of electrodeposited ceria thin films. Thin Solid Films. 2011;519:3538-3543. DOI: 10.1016/j.tsf.2011.01.245.

[108] Khalipova OS, Lair V, Ringuede A. Electrochemical synthesis and characterization of gadolinia-doped ceria thin films. Electrochim. Acta. 2014;116:183-187. DOI: 10.1016/j.electacta.2013.11.022.

[109] Qu D, Xie F, Meng H, Gong L, Zhang W, Chen J, Li G, Liu P, Tong Y. Preparation and characterization of nanocrystalline CeO_2-Tb_2O_3 films obtained by electrochemical deposition method. J. Phys. Chem. C. 2010;114:1424-1429. DOI: 10.1021/jp907628g.

[110] Lair V, Zivkovic LS, Lupan O, Ringuede A. Synthesis and characterization of electrodeposited samaria and samaria-doped ceria thin films. Electrochim. Acta. 2011;56:4638-4644. DOI: 10.1016/j.electacta.2011.02.101.

[111] Aghazadeh M, Yousefi T. Preparation of Gd_2O_3 nanorods by electrodeposition-heat-treatment method. Mater. Lett. 2012;73:176-178. DOI: 10.1016/j.matlet.2012.01.009.

[112] Abed F, Aghazadeh M, Arhami B. Preparation of Gd_2O_3 coral-like nanostructures by pulse electrodeposition-heat-treatment method. Mater. Lett. 2013;99:11-13. DOI: 10.1016/j.matlet.2013.02.025.

[113] Lu X, Li G, Yu X, Tong Y. Electrochemical synthesis and characterization of TbO_{2-x} flowerlike nanostructures. Electrochem. Solid-State Lett. 2008;11:K85-K88. DOI: 10.1149/1.2945878.